CHAPTER V
HYDROGEN PRODUCTION FROM PHOTOCATALYTIC WATER SPLITTING OVER MESOPOROUS-ASSEMBLED $SrTiO_3$ NANOCRYSTAL-BASED PHOTOCATALYSTS

Abstract

Mesoporous-assembled $SrTiO_3$ nanocrystal-based photocatalysts were synthesized via the sol-gel method with the aid of a structure-directing surfactant. The photocatalytic water splitting activity for hydrogen production over the mesoporous-assembled $SrTiO_3$ nanocrystal-based photocatalysts with various hole scavengers: methanol, ethanol, 2-propanol, D-glucose, and Na_2SO_3, was investigated. The pristine mesoporous-assembled $SrTiO_3$ photocatalysts exhibited much higher photocatalytic activity in hydrogen production via the photocatalytic water splitting using methanol as the hole scavenger than both non-mesoporous-assembled commercial photocatalysts: commercial $SrTiO_3$ and commercial TiO_2 (Degussa P-25), even if their specific surface areas were lower than those of both commercial photocatalysts. These results point out that the mesoporous assembly of nanocrystals with high pore uniformity plays a significant role, affecting the photocatalytic hydrogen production activity of the $SrTiO_3$ photocatalysts. The Pt co-catalyst enhances the visible-light harvesting ability of the mesoporous-assembled $SrTiO_3$ photocatalyst and behaves as the active site for proton reduction, leading to photocatalytic activity enhancement under both UV and visible light irradiation. Methanol provided the highest photocatalytic hydrogen production enhancement. An optimum Pt loading of 0.5 wt.% on the mesoporous-assembled $SrTiO_3$ photocatalyst provided the highest photocatalytic activity, with hydrogen production rates (from 50 vol.% methanol aqueous solution systems) of 276 and 188 μmol h^{-1} g_{cat}^{-1} and quantum efficiencies of 1.9 and 0.9 % under UV and visible light irradiation, respectively.

To be published in Journal of Molecular Catalysis A: Chemical, 312 (2009) 97-106

5.1 Introduction

Photocatalytic water splitting reaction originates by the direct absorption of photons by a photocatalyst. A photocatalyst can be excited by photons with energy equal to or higher than its band gap energy, and then the photo-generated electrons and holes directly contribute to the decomposition of water into H_2 and O_2 [1]. It has been suggested that a photocatalyst can accelerate the water splitting reaction if its conduction and valence bands are located at appropriate potential levels, i.e. the conduction band should be more negative than the proton reduction potential level, and the valence band should be more positive than the water oxidation potential level [2,3]. The photo-generated electrons and holes that can migrate to the photocatalyst surface will reduce protons to H_2 and oxidize water to O_2. However, the photo-generated electrons and holes can recombine both in the bulk phase and on the photocatalyst surface in a very short time [1], resulting in lowering the photocatalytic hydrogen production efficiency. In addition, because the decomposition of water into H_2 and O_2 is an energy-consuming process, the backward reaction of H_2 and O_2 to H_2O tends to occur preferentially [4-8], also resulting in low photocatalytic efficiency. Therefore, it is difficult to achieve photocatalytic hydrogen production from pure water. Adding some specific chemicals as hole scavengers into the water can offer simultaneously both photo-generated electron-hole separation and backward reaction suppression [9-15], resulting in photocatalytic activity enhancement. Various types of hole scavengers have been studied for the enhancement of hydrogen production from the photocatalytic water splitting [9-17].

Perovskite-type $SrTiO_3$ has been used in photocatalytic water splitting for hydrogen production because its band structure suits the water redox potential levels. The redox potentials of the photo-generated electrons and holes of $SrTiO_3$ are powerful enough to facilitate hydrogen and oxygen formation [18-20]. In addition, $SrTiO_3$ has been shown to possess good structure stability as a host for metal loading [21, 22]. Our previous work revealed that the mesoporous-assembled structure of $SrTiO_3$ nanocrystals can enhance the photocatalytic activity for methyl orange photodegradation [23]. The photocatalytic activity enhancement by mesoporous-

structured photocatalysts has also been studied and is confirmed by several articles [24-28].

According to the aforementioned observations, the objective of this work was to focus on the development of effective $SrTiO_3$ photocatalysts for hydrogen production via photocatalytic water splitting. In this present work, photocatalytic water splitting over pristine mesoporous-assembled $SrTiO_3$ nanocrystal and Pt-loaded mesoporous-assembled $SrTiO_3$ nanocrystal photocatalysts was investigated comparatively. The performance of various hole scavengers on the photocatalytic hydrogen production activity over the $SrTiO_3$ photocatalysts was also studied in order to obtain the best hole scavenger for the photocatalytic hydrogen production system. According to literature, alcohol is the most widely used hole scavenger, and it shows good photocatalytic hydrogen activity enhancement [13, 25, 26, 29-31]. In addition, Na_2SO_3 is widely used as an oxygen scavenger in many applications, such as feedwater treatment to prevent corrosion [32], wastewater treatment [33], and photocatalytic hydrogen production [34]. Moreover, it has been suggested that D-glucose, a biomaterial, that is a building unit of all biomasses and that has high H content in its molecule, may be an effective hole scavenger. Therefore, this work also investigates the effectiveness of these hole scavengers (alcohol, Na_2SO_3, and D-glucose) on the photocatalytic hydrogen production activity of the studied photocatalytic system. In addition, the dependence of the apparent activation energy and the photocatalytic enhancement ability on the methanol content (the most effective hole scavenger) and reaction temperature was examined.

5.2 Experimental

5.2.1 Materials

Strontium nitrate ($Sr(NO_3)_2$, Merck Co., Ltd.), tetraisopropyl orthotitanate (TIPT, Merck Co., Ltd.), acetylacetone (ACA, S.D. Fine-Chem Ltd.), laurylamine (LA, Merck Co., Ltd.), hydrochloric acid (HCl, 37% analytical grade, Labscan Asia Co., Ltd.), and anhydrous ethyl alcohol (EtOH, Italmar Co., Ltd.) were used as starting materials for the mesoporous-assembled $SrTiO_3$ photocatalyst synthesis. Chloroplatinic acid ($H_2PtCl_6 6H_2O$, Aldrich Co., Ltd.) was used as a Pt

precursor. Anhydrous methyl alcohol (MeOH, 99.8 % purity, Labscan Asia Co., Ltd.), anhydrous ethyl alcohol (EtOH, 99.5 % purity, Italmar Co., Ltd.), anhydrous iso-propyl alcohol (2-PrOH, BDH Laboratory Co., Ltd.), D-glucose (Ajax Finechem), and sodium sulfite (Na_2SO_3, Riedel-Dehaeh) were used as hole scavengers for the photocatalytic hydrogen production activity investigation. Commercially available $SrTiO_3$ nanopowder (Wako Pure Chemical Industries, Ltd.) and TiO_2 nanopowder (Degussa P-25, Tokyo Chemical Industry Co., Ltd.) were also used for the comparative study on photocatalytic hydrogen production activity. All chemicals used in this study were used as received, without further purification.

5.2.2 Synthesis Procedure of Mesoporous-Assembled $SrTiO_3$ Photocatalysts

The mesoporous-assembled $SrTiO_3$ nanocrystal photocatalysts, with and without Pt loading, were synthesized via the sol-gel process with the aid of a structure-directing surfactant under mild conditions [23]. An ACA/TIPT solution was prepared by adding 2.00 g of ACA to 5.68 g of TIPT at an equimolar proportion. A laurylamine hydrochloride (LAHC) solution was prepared by dissolving 1.02 g of LA with an equimolar HCl (0.09 g) in 50 cm^3 of EtOH. Then, 4.23 g of $Sr(NO_3)_2$ was added to the LAHC solution with continuous stirring to obtain a clear solution of LAHC/$Sr(NO_3)_2$. For the case of the Pt-loaded mesoporous-assembled $SrTiO_3$ nanocrystal photocatalyst synthesized, $H_2PtCl_6 6H_2O$ of various amounts was added to the LAHC/$Sr(NO_3)_2$ solution to obtain different Pt loadings, as being analogous to Pt-loaded mesoporous-assembled TiO_2 synthesized by the single-step sol-gel process [28]. Afterwards, the LAHC/$Sr(NO_3)_2$ or LAHC/$Sr(NO_3)_2$/$H_2PtCl_6 6H_2O$ solution was slowly dropped into the ACA/TIPT solution while stirring continuously to obtain the ACA/TIPT/LAHC/$SrTiO_3$ or ACA/TIPT/LAHC/$SrTiO_3$/$H_2PtCl_6 6H_2O$ solution with a LAHC-to-TIPT molar ratio of 0.25:1 and a Sr-to-Ti molar ratio of 1:1. Next, the resultant mixture was incubated at 80°C for 1 d to obtain complete gel formation. The resulting gel was further dried at 80°C for 2 d. Finally, the dried gel was calcined at 700°C with a heating rate of 1°C min^{-1}, and after reaching 700°C, it was maintained for 4 h to remove the surfactant and the remaining solvent from the

dried gel to yield the mesoporous-assembled $SrTiO_3$ nanocrystal photocatalyst (the pristine $SrTiO_3$) or the Pt-loaded mesoporous-assembled $SrTiO_3$ nanocrystal photocatalyst (the Pt-loaded $SrTiO_3$).

5.2.3 Photocatalyst Characterization Techniques

The crystallinity and purity of the synthesized and commercial photocatalysts were examined by X-ray diffraction (Rigaku, RINT-2100) with a rotating anode XRD generating monochromated CuK_α radiation using the continuous scanning mode at a rate of 2°C min^{-1} and operating conditions of 40 kV and 40 mA. The crystallite size (D) was calculated from the line broadening of the corresponding X-ray diffraction peak according to the Debye-Scherrer equation [35]:

$$D = \frac{K\lambda}{\beta\cos(\theta)}$$

where K is the Scherrer constant (0.89), λ is the wavelength of the X-ray radiation (0.15418 nm for CuK_α), β is the full width half maximum (FWHM) of the diffraction peak measured at 2θ, and θ is the diffraction angle.

The photocatalyst morphologies and the existence of the loaded Pt were observed by a transmission electron microscope (TEM) (JEOL, JEM-200CX) at 200 kV. The specimens for TEM analysis were prepared by ultrasonically dispersing pestled powders of the photocatalysts in 2-propanol and then placing drops of the suspension onto a Cu microgrid coated with a carbon film.

The N_2 adsorption–desorption isotherms of the photocatalysts were obtained by using a nitrogen adsorption–desorption apparatus (BEL Japan, BELSORP-18 PLUS) at a liquid nitrogen temperature of -196°C. The Brunauer-Emmett-Teller (BET) approach, using adsorption data over the relative pressure ranging from 0.05 to 0.35, was employed to determine the specific surface areas of the studied photocatalysts. The Barrett-Joyner-Halenda (BJH) approach, using the desorption data, was used to obtain their mean pore size and pore size distribution.

The diffuse reflectance spectra of the synthesized and commercial photocatalysts were obtained by using a UV-Visible spectrophotometer (Shimadzu, UV-2450) at room temperature with $BaSO_4$ as the reference. Afterwards, the diffuse

reflectance spectra were analyzed to estimate the band gap energy (E_g, eV) by using the Kubelka-Munk function (F(r)), as expressed by the following equation [36]:

$$F(r) = \frac{(1-r)^2}{2r}$$

where r is the ratio of the reflected light intensity to the reflected light intensity of the reference. The band gap wavelength (λ_g, nm) was the wavelength at the crossing point between the line extrapolated from the onset of the rising part and the x-axis of the plot of F(r) as a function of wavelength (λ, nm). The E_g was then determined by using the following equation [36]:

$$E_g = \frac{1240}{\lambda_g}$$

The estimated error of Eg determination was found to be ±0.02 eV with a standard deviation of 0.7%.

The actual Pt loading of the investigated $SrTiO_3$ photocatalysts was analyzed by an X-ray fluorescence spectroscope (Phillip, WD-XRF PW-2400). The aggregated particle size distribution of the investigated $SrTiO_3$ photocatalysts was analyzed by a light scattering particle size analyzer (laser technique) (Malvern / Mastersizer X, Malvern Instruments Ltd.), capable to measure in the range of 0.1 to 600 μm with the standard deviation of the mean aggregated particle size in the range of -9 to 9 μm.

The oxidation state of the loaded Pt was analyzed by an X-ray photoelectron spectroscope (XPS) (Physical Electronics, PHI 5800 ESCA). A monochromatic Al Kα source emitting an X-ray energy of 1,486.6 eV was used as the X-ray source. The relative surface charging of the samples was removed by referencing all the energies to the C1s level as an internal standard at 284.8 eV

5.2.4 Photocatalytic Water Splitting Experiments

The photocatalytic activity of the synthesized and commercial $SrTiO_3$ photocatalysts for the water splitting reaction was investigated by using the average hydrogen production rate during the first 5 h irradiation period as an indicator. The photocatalytic water splitting experiment was performed in an outer-irradiation and air-tight Pyrex glass reactor (750 ml), connected to a water-cooling system. A set of

176 W Hg lamps (16 lamps, TUV 11 W PL-S, Phillip), which emitted light of more than 95% with a wavelength of 254 nm with total irradiance of 2.3 mW cm^{-2}, and a 300 W Xe lamp (KXL-300, Wacom Electric) combined with a UV cutoff filter (ATG, B-485), which allowed only the visible light with wavelengths longer than 400 nm to pass with total irradiance of 2.6 mW cm^{-2}, were employed as UV and visible light sources, respectively. In a typical experiment, a constant photocatalyst dosage of 1×10^{-3} g cm^{-3} was suspended in an aqueous solution with different hole scavengers by using a magnetic stirrer. Prior to the reaction testing, the suspension was left in the dark while simultaneously being thoroughly deaerated by purging with Ar gas for 20 min, and then the suspension was irradiated by turning on the lamps for 5 h. For the UV irradiation, the reaction temperature was controlled at three levels: 15, 30, and 45°C. For the visible light irradiation, the reaction was performed at room temperature of 27°C. A gas sample in the headspace of the studied reactor was periodically withdrawn at 1 h intervals and analyzed for its hydrogen, oxygen, carbon dioxide, and carbon monoxide concentrations by using a gas chromatograph (Hayesep D100/120, PERKIN ELMER) equipped with a thermal conductivity detector (TCD). The average hydrogen production rate during the first 5 h irradiation period was used to determine the quantum efficiency (QE) of the studied systems. The quantum efficiency (QE) was calculated by using the following equation:

$$QE = \frac{\text{Combustion energy of produced hydrogen}}{\text{Irradiating photon energy}}$$

$$QE = \frac{H_{c,H2}\ (J\cdot mol^{-1}) \times \text{Hydrogen production rate}\ (mol\cdot h^{-1})}{\text{Total irradiance}\ (J\cdot h^{-1}\cdot cm^{-2}) \times \text{Irradiated area}\ (cm^2)} \times 100\%$$

where $H_{c,H2}$ is the heat of combustion of hydrogen gas ($J\cdot mol^{-1}$).

Moreover, the dependence data of the initial rate of hydrogen production for the first 0.5 h irradiation time of the system operated at different MeOH concentrations and reaction temperatures were used to determine the apparent activation energy ($\hat{E}_a$, kJ mol^{-1}) of the photocatalytic water splitting reaction based

on two reaction temperature ranges: a low temperature range of 15 to 30°C (varying from 15, 20, 25, to 30°C) and a high temperature range of 30 to 45°C (varying from 30, 35, 40, to 45°C). The $\hat{E}_a$ values of all systems were calculated based on the Arrhenius equation. The $\hat{E}_a$ value was determined from the slope of the natural log of the initial rate of hydrogen production as a function of the reciprocal of the temperature, with the square of correlation coefficient (R^2) in the range of 0.97 to 0.99. The $\hat{E}_a$ value was then calculated by using the following equation:

$$\hat{E}_a = (-1) \times (\text{slope} \times R)$$

where R is the gas constant, 8.314 J mol^{-1} K^{-1}.

5.3 Results and Discussion

5.3.1 Photocatalyst Characterization Results

The XRD patterns of the pristine $SrTiO_3$, the 0.5 wt.% Pt-loaded $SrTiO_3$, and the commercial $SrTiO_3$ are shown in Figure 5.1. All investigated photocatalysts showed the single $SrTiO_3$ phase, which is a cubic perovskite-type structure (JCPDS card No. 35-0734) [37], with high purity. The presence of the Pt co-catalyst phase was not observed by the XRD analysis. This is possibly due to the low loading and the high dispersion degree with small particle sizes of Pt throughout the mesoporous-assembled network. The crystallite sizes of all the photocatalysts, calculated from their XRD patterns, are 35, 35, and 33 nm for the pristine $SrTiO_3$, the 0.5 wt.% Pt-loaded $SrTiO_3$, and the commercial $SrTiO_3$, respectively (Table 5.1). Table 5.1 presents a comparison of the physical and textural properties of the synthesized $SrTiO_3$ and the commercial $SrTiO_3$. The XRD results suggest that the addition of Pt does not affect the crystallite size of $SrTiO_3$. In addition, the estimated particle sizes, from their TEM images (Figures 5.2(a)-5.2(c)), are 20–40 nm for both the pristine $SrTiO_3$ and the 0.5 wt.% Pt-loaded $SrTiO_3$, and 20–200 nm for the commercial $SrTiO_3$. From the results of the size analysis from those two methods, the estimated particle size of the synthesized $SrTiO_3$ obtained from the TEM analysis was close to the crystallite size calculated from the XRD pattern, indicating that the

synthesized $SrTiO_3$ photocatalysts have a single crystal structure, while this was not the case for the commercial $SrTiO_3$.

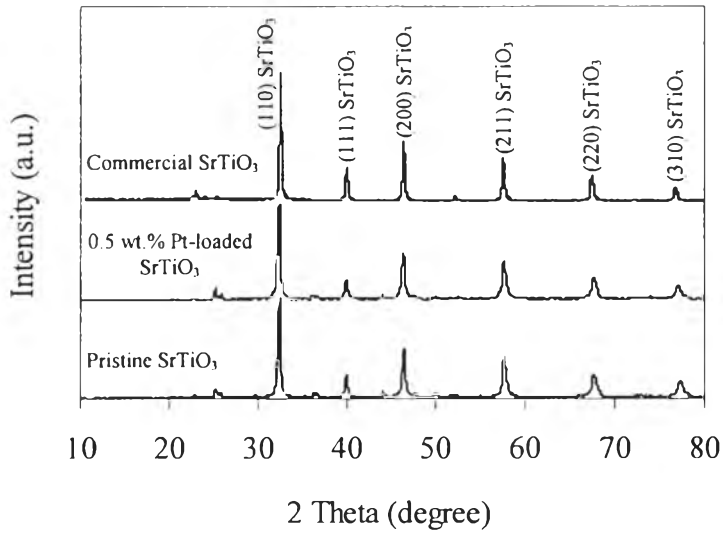

Figure 5.1 XRD patterns of the $SrTiO_3$ photocatalysts.

Table 5.1 Physical and textural properties of all investigated photocatalysts

Photocatalyst	Pt loading (wt.%)	Actual Pt loading (wt.%)	Crystallite size (nm)	BET surface area (m^2g^{-1})	Mean mesopore diameter (nm)	Total pore volume (mm^3g^{-1})	E_g (eV)
Pristine $SrTiO_3$	-	-	35	8-12	4.6-4.8	40-85	3.23
Pt-loaded $SrTiO_3$	0.1	0.1	35	8-12	4.5-4.8	40-85	3.16
	0.5	0.43	35	8-12	4.5-4.8	40-85	3.16
	1.0	0.91	35	8-12	4.4-4.8	40-85	3.16
	1.5	1.52	35	8-12	4.3-4.7	40-85	3.16
Commercial $SrTiO_3$	-	-	33	28-32	72-74	180-250	3.38

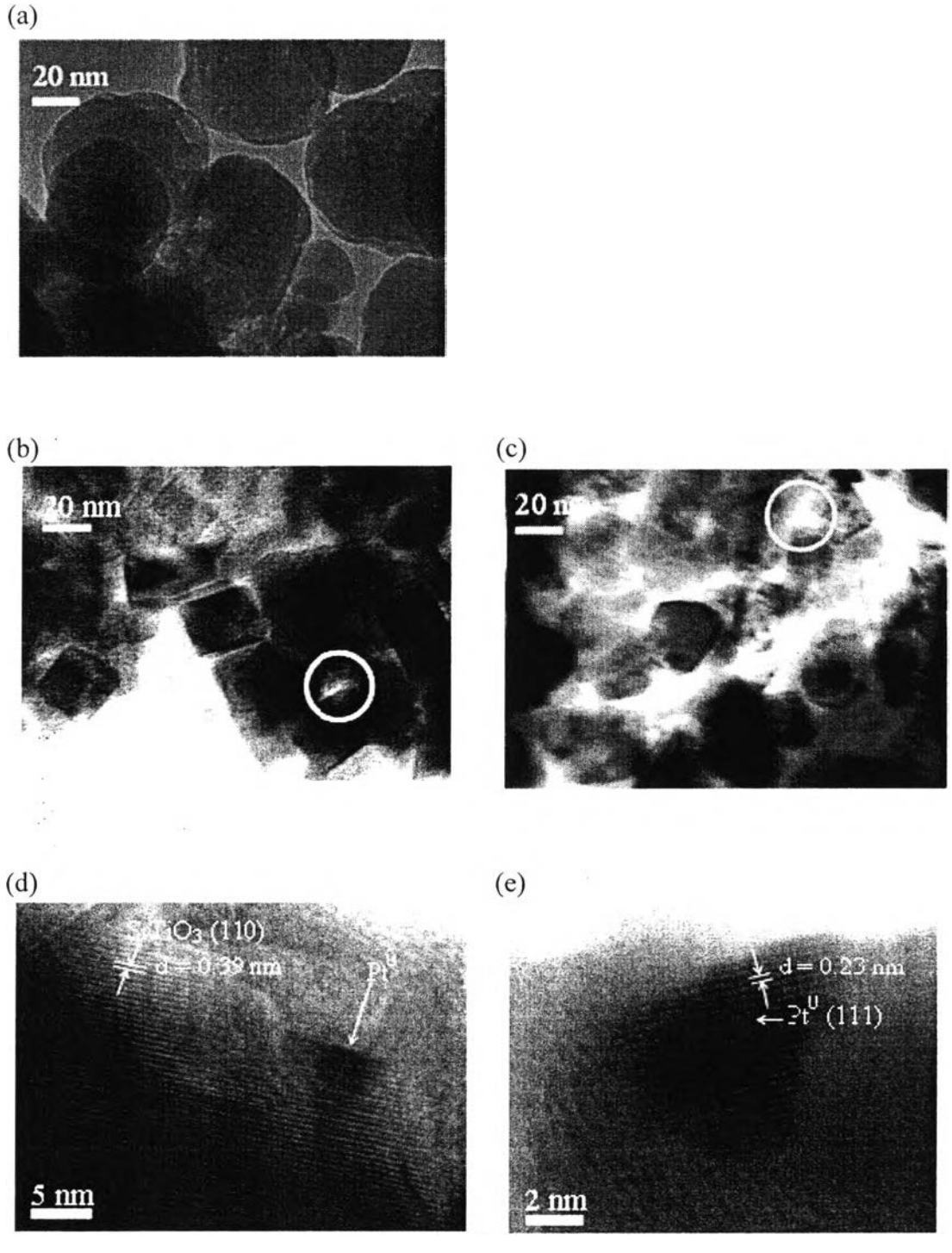

Figure 5.2 TEM images of the $SrTiO_3$ photocatalysts: (a) commercial $SrTiO_3$, (b) pristine $SrTiO_3$, (c) 0.5 wt.% Pt-loaded $SrTiO_3$, and HRTEM images of the 0.5 wt.% Pt-loaded $SrTiO_3$ to show (d) d spacing of $SrTiO_3$ (110) and (e) d spacing of Pt^0 (111).

It can be seen for the TEM images that the synthesized $SrTiO_3$ photocatalysts have a much more uniform particle size than that of the commercial one and clearly exhibit the mesoporous structure (pore diameter between 2 and 50 nm) formed between the $SrTiO_3$ nanocrystals due to their assembly, as marked by a circle in Figures 5.2(b) and 5.2(c); these are important characteristics of the synthesized $SrTiO_3$ photocatalyst for the enhancement of the photocatalytic activity [23]. The porous structure of the synthesized $SrTiO_3$ can be identified by the N_2 adsorption–desorption isotherms (Figures 5.3(a) and 5.3(b)) as their isotherms show a type IV IUPAC pattern with a hysteresis loop, implying that they mainly consist of well-developed mesopores in their assembled framework [38]. Both mesoporous-assembled $SrTiO_3$ photocatalysts (the pristine $SrTiO_3$ and the Pt-loaded $SrTiO_3$) exhibit high pore uniformity, according to their very narrow pore size distributions, as shown in Figures 5.3(a) and 5.3(b). In contrast, the commercial $SrTiO_3$ has a non-uniform particle size (Figures 5.2(a), 5.3(c), and 5.4) with an average particle size much larger than its crystallite size (Table 5.1 and Figure 5.4). From the adsorption–desorption isotherm results, the commercial $SrTiO_3$ shows a type II IUPAC pattern without a hysteresis loop with a very broad pore size distribution, mainly in the macropore region (pore diameter > 50 nm) (Figure 5.3(c)). However, the BET surface area of the commercial $SrTiO_3$ photocatalyst is higher than those of both the pristine $SrTiO_3$ and the Pt-loaded $SrTiO_3$ photocatalysts, as shown in Table 5.1.

From the results, the addition of Pt to the synthesized $SrTiO_3$ did not significantly affect the purity, the specific surface area, the pore characteristics, the crystallite size, and the aggregated particle size (Table 5.1 and Figure 5.4). The high-resolution TEM (HRTEM) images (Figures 5.2(d) and 5.2(e)) show the oriented and ordered lattice fringes for $SrTiO_3$ photocatalyst and Pt nanoparticle, respectively. The d spacing values indicate that the loaded Pt exists as the metal form with the d spacing value of 0.23 nm corresponding to the cubic Pt^0 (111) lattice parameter [39] and likely exists as a separate phase on the $SrTiO_3$ surface because the d spacing value of the $SrTiO_3$ dose not change with the value of 0.39 nm corresponding to the cubic perovskite $SrTiO_3$ (110) lattice parameter [20, 40].

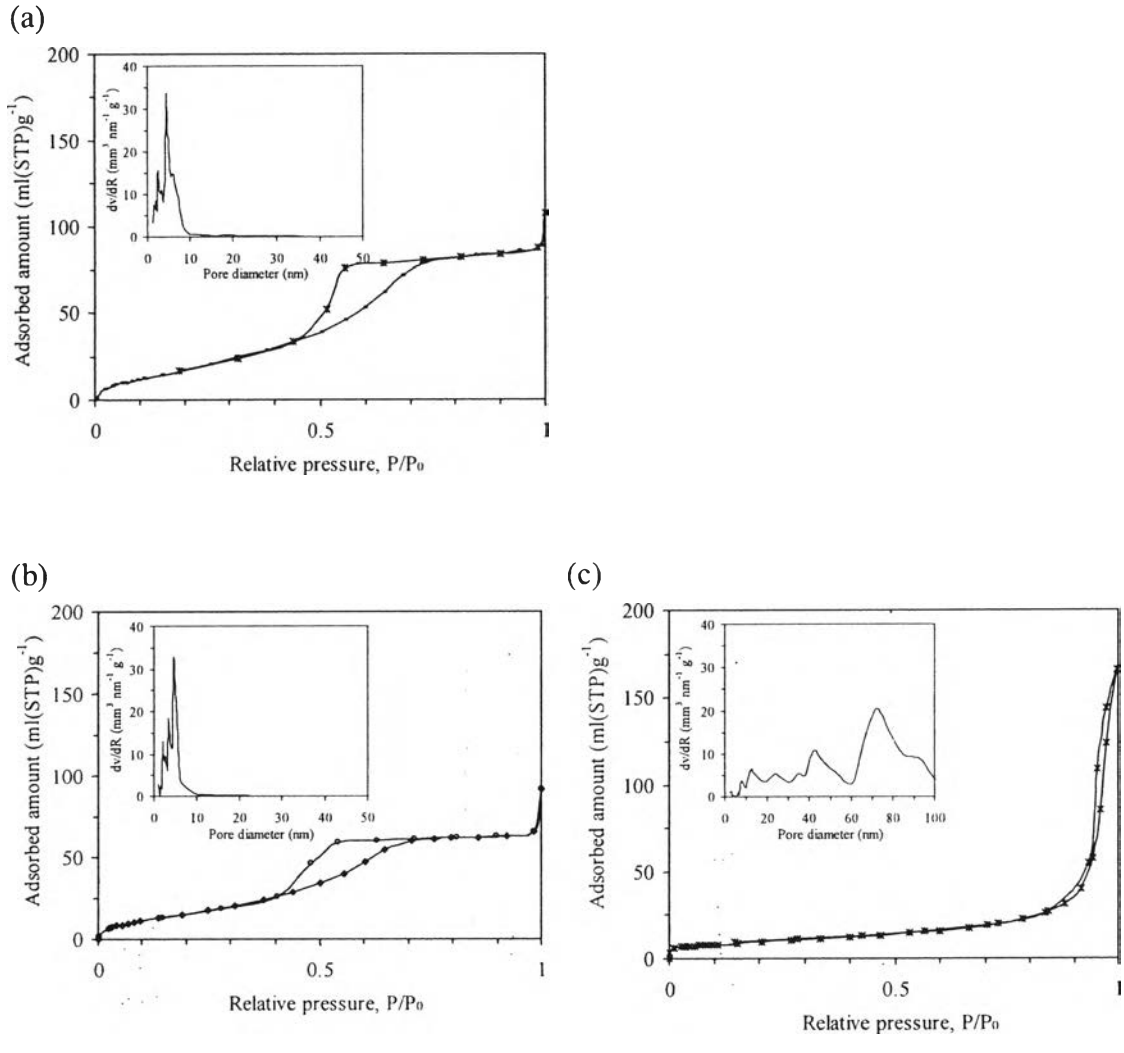

Figure 5.3 N_2 adsorption-desorption isotherm and pore size distribution (inset) of (a) the pristine mesoporous-assembled $SrTiO_3$ photocatalyst, (b) the 0.5 wt.% Pt-loaded $SrTiO_3$, and (c) the commercial $SrTiO_3$.

The metallic form of the loaded Pt was confirmed by the deconvoluted Pt4f XPS spectra of the 0.5 wt.% Pt-loaded $SrTiO_3$ photocatalyst, as shown in Figure 5.5. The spectra shows doublet peaks appeared at 72.5 and 75.6 eV, which can be attributed to the $Pt4f_{7/2}$ and $Pt4f_{5/2}$ levels of Pt^0 oxidation state, respectively [41]. This suggests that the loaded Pt on the $SrTiO_3$ photocatalyst was in the metallic form.

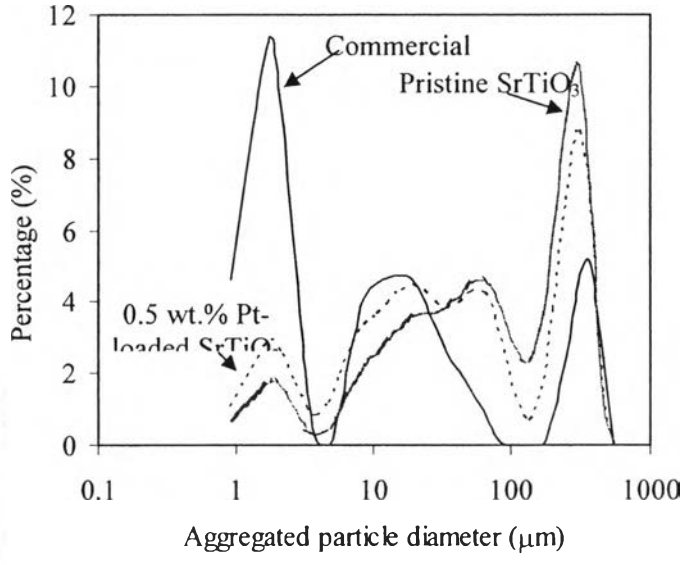

Figure 5.4 Aggregated particle size distributions of the commercial $SrTiO_3$ and the mesoporous-assembled $SrTiO_3$ photocatalysts: pristine $SrTiO_3$ and 0.5 wt.% Pt-loaded $SrTiO_3$.

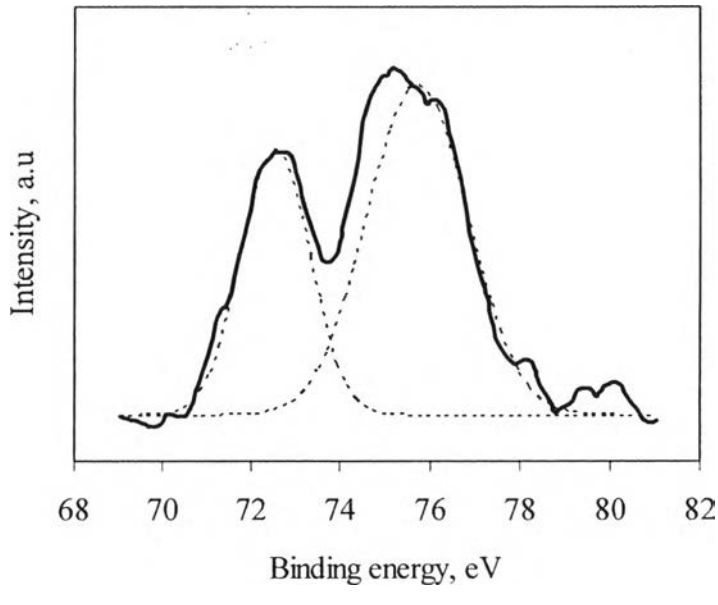

Figure 5.5 Deconvoluted Pt4f XPS spectra of the 0.5 wt.% Pt-loaded $SrTiO_3$ photocatalyst.

According to the reflectance spectra results, i.e. the Kubelka-Munk function plots of the pristine and the 0.5 wt.% Pt-loaded $SrTiO_3$ photocatalysts (Figure 5.6), they clearly indicate that the addition of Pt on the $SrTiO_3$ surface can enhance the visible-light harvesting ability and increase the band gap wavelength (λ_g) of the synthesized $SrTiO_3$ photocatalyst, leading to the decrease in the band gap energy from 3.23 to 3.16 eV (Table 5.1). The presence of a Pt metal at the surface of $SrTiO_3$ possibly results in the formation of a Schottky barrier at the Pt–$SrTiO_3$ interface, which decreases the energy position of the $SrTiO_3$ conduction band to its minimum potential level, leading to a decrease in the band gap energy of the synthesized $SrTiO_3$ photocatalyst [42, 43].

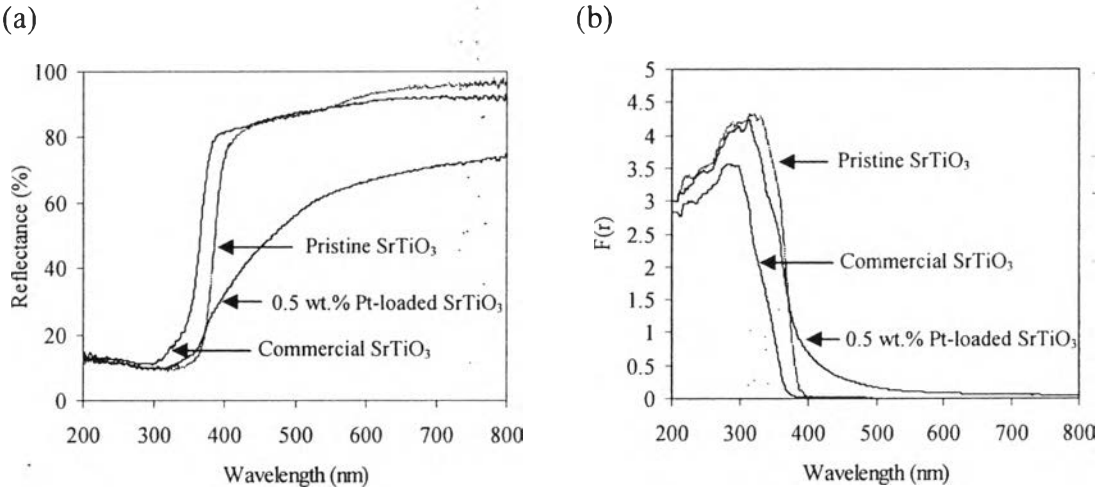

Figure 5.6 Plot of (a) reflectance and (b) F(r) as a function of wavelength of the commercial $SrTiO_3$ and the mesoporous-assembled $SrTiO_3$ photocatalysts: pristine $SrTiO_3$ and 0.5 wt.% Pt-loaded $SrTiO_3$.

5.3.2 Effects of Type and Concentration of Hole Scavenger

The effects of type and concentration of hole scavengers on the photocatalytic hydrogen production activity over the 0.5 wt.% Pt-loaded mesoporous-assembled $SrTiO_3$ nanocrystal photocatalyst were studied. The enhancement of the photocatalytic activity of the studied photocatalyst by adding different hole scavengers was found in the following order: MeOH > EtOH > D-glucose > 2-PrOH > Na_2SO_3 (Figure 5.7). In the case of Na_2SO_3, $CoCl_2$ was added as

a catalyst to accelerate the rate of the reaction between Na_2SO_3 and O_2 to form Na_2SO_4, resulting in the suppression of the backward reaction. The use of MeOH provided the highest photocatalytic enhancement ability (the ability to increase the photocatalytic hydrogen production activity), as compared to the other studied hole scavengers, possibly because it has the highest ability to donate electrons to scavenge the valence band holes to preventing photo-generated charge recombination [44, 45]. In a comparison among alcohols, the photocatalytic activity tended to increase with increasing alcohol concentration. For MeOH as the hole scavenger, the hydrogen production rate significantly increased in the MeOH concentration range of 0-20 vol.%; beyond this range, it only slightly increased. Because the MeOH had the highest photocatalytic enhancement ability, it was selected as the hole scavenger in further investigations.

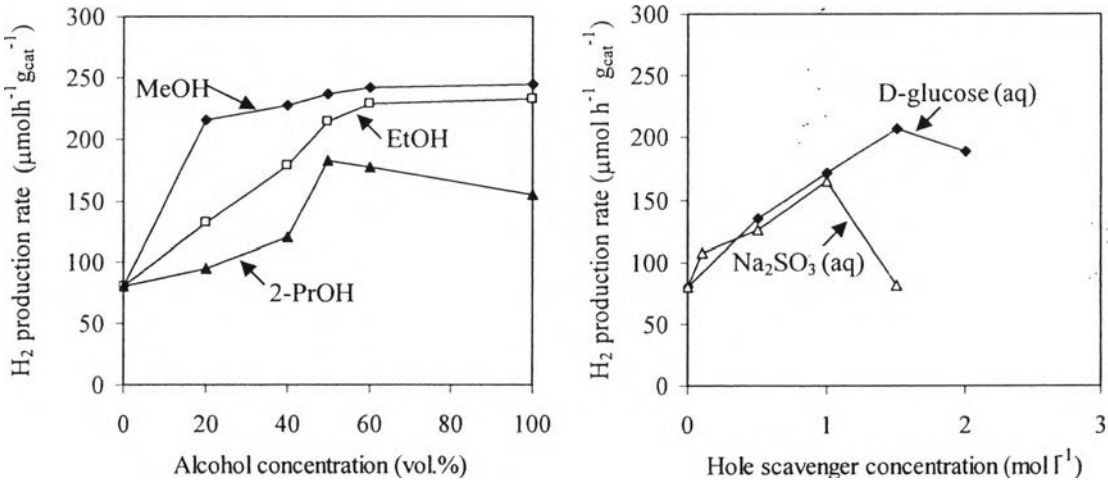

Figure 5.7 Dependence of H_2 production rate over the 0.5 wt.% Pt-loaded $SrTiO_3$ photocatalyst under UV irradiation on type and concentration of hole scavengers (studied conditions: 5 h irradiation time, 500 ml of aqueous solution, 0.5 g of photocatalyst, reaction temperature of 15°C).

The results of the set of preliminary experiments performed to determine the effects of MeOH concentration, the presence of the 0.5 wt.% Pt-loaded $SrTiO_3$ photocatalyst, and temperature on the photocatalytic activity in hydrogen production are shown in Figure 5.8. For all studied systems, no hydrogen was

produced under dark conditions. In the case of no photocatalyst addition under light irradiation at two reaction temperatures of 15 and 45°C, hydrogen was produced from the pure MeOH system and the 50 vol.% MeOH aqueous solution system, but was not observed from the pure H_2O system (Figure 5.8), indicating that MeOH itself can be decomposed by 0the photolysis into hydrogen. However, in the presence of the 0.5 wt.% Pt-loaded mesoporous-assembled $SrTiO_3$ nanocrystal photocatalyst, hydrogen production by the photocatalysis was much higher than that by the photolysis. Moreover, it is clear that the investigated photocatalyst had lower photocatalytic activity in the pure H_2O system, as compared with the pure MeOH system and the 50 vol.% MeOH aqueous solution system.

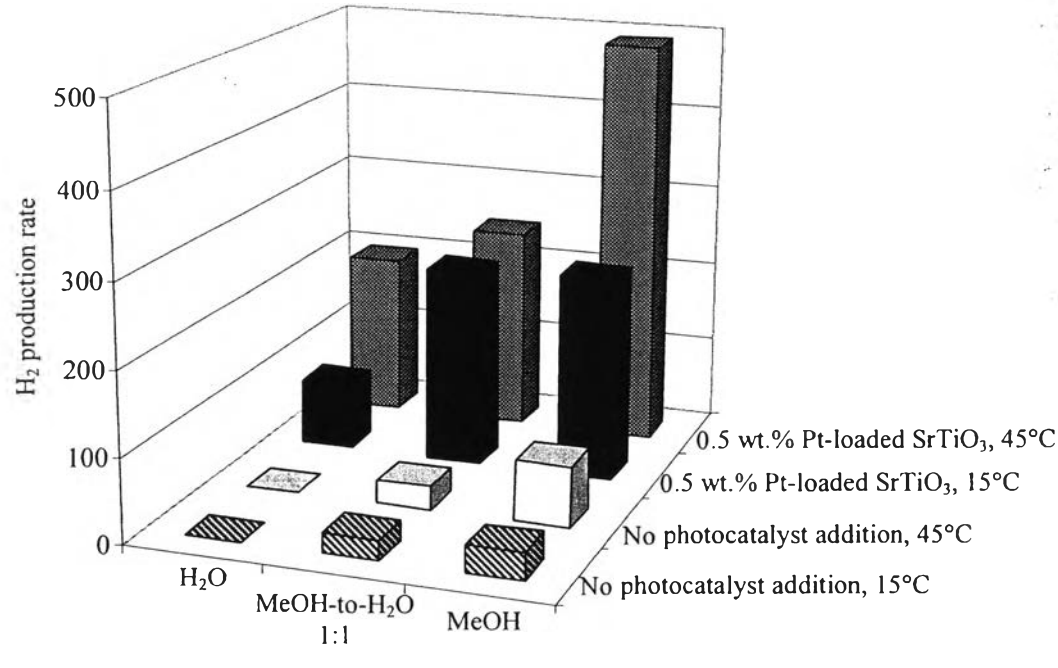

Figure 5.8 Effects of the reactant system, the presence of a photocatalyst, and the reaction temperature on H_2 production (the overall rate of reaction at 5 h, 500 ml of solution, 0.5 g of 0.5 wt. % Pt-loaded $SrTiO_3$ photocatalyst, and UV irradiation). Note: the units of the H_2 production rate is μmol h^{-1} or μmol h^{-1} g_{cat}^{-1} in the case of no photocatalyst addition and in the case of photocatalyst addition, respectively.

These experimental results confirm that the use of MeOH as a hole scavenger can greatly enhance the photocatalytic hydrogen production activity of the studied photocatalyst. The results show that the photocatalytic activity in hydrogen production increased with increasing temperature from 15 to 45°C, and the temperature affected the pure H_2O system (without MeOH as the hole scavenger) more than the MeOH-H_2O systems.

5.3.3 Effect of Pt Loading

In this experimental part, the photocatalytic activity of the pristine mesoporous-assembled $SrTiO_3$ photocatalyst for hydrogen production via the photocatalytic water splitting using methanol as the hole scavenger was first comparatively investigated with that of two non-mesoporous-assembled photocatalysts: the commercial $SrTiO_3$ and the reported highly active commercial TiO_2 (P-25, specific surface area of 51.6 m^2 g^{-1}, crystallite sizes of 21 and 30 nm for the anatase and rutile phases (mixed phase), respectively). The results show that the synthesized mesoporous-assembled $SrTiO_3$ photocatalyst exhibited significantly higher photocatalytic activity under UV irradiation than both the commercial $SrTiO_3$ and TiO_2 photocatalysts (the hydrogen production rates of 156, 46, and 37 μmol h^{-1} g_{cat}^{-1}, for mesoporous-assembled $SrTiO_3$, commercial $SrTiO_3$, and commercial TiO_2 (P-25), respectively), even if the synthesized photocatalyst had lower specific surface areas when compared with the commercial photocatalysts (Table 5.1). This is possibly because the reactants and all products of this water splitting reaction have small molecular sizes, which can easily diffuse through either mesopore or macropore, but the mesoporous structure more efficiently provides the active site accessibility on the photocatalyst surface for the reactants, as compared to the macroporous one. Therefore, mesoporous-assembled structure of the nanocrystals with a high pore uniformity of the $SrTiO_3$ photocatalyst plays a significant role in the enhancement of the photocatalytic activity for hydrogen production via the photocatalytic water splitting.

The synthesized mesoporous-assembled $SrTiO_3$ photocatalyst was used for the further investigation on the Pt co-catalyst loading effect on the photocatalytic activity in hydrogen production to determine the optimum amount of

Pt to be incorporated into the mesoporous-assembled $SrTiO_3$ nanocrystal photocatalyst. Figure 5.9 illustrates the H_2 production rate under UV and visible light irradiation of the mesoporous-assembled $SrTiO_3$ nanocrystal photocatalysts with various Pt loadings.

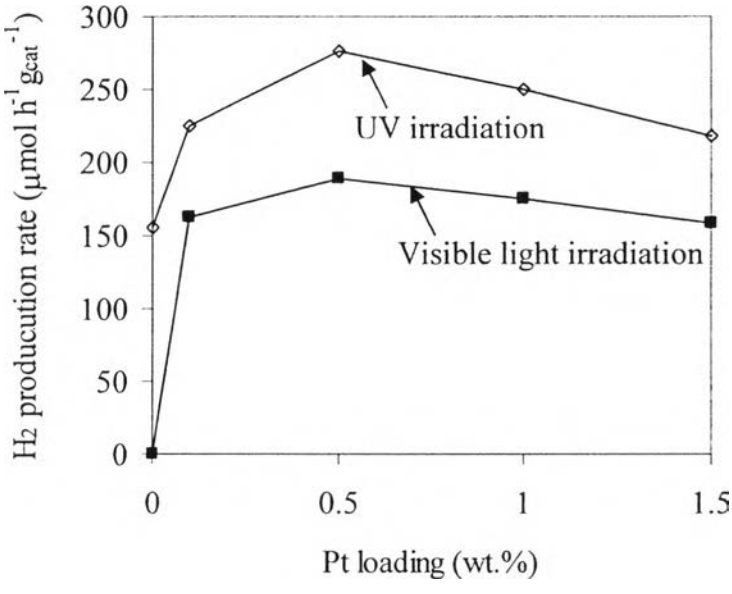

Figure 5.9 H_2 production rate under UV and visible light irradiation as a function of Pt loading over the synthesized $SrTiO_3$ (studied conditions: 5 h irradiation time, 500 ml of 50 vol.% MeOH aqueous solution, 0.5 g of photocatalyst, reaction temperatures of 45°C for UV irradiation and 30°C for visible light irradiation).

The comparative results of the photocatalytic activity of the pristine $SrTiO_3$ and the Pt-loaded $SrTiO_3$ indicate that the presence of Pt on the $SrTiO_3$ photocatalyst surface can enhance the photocatalytic activity of the synthesized $SrTiO_3$ photocatalyst under both UV and visible light irradiation. This is possibly due to the roles of Pt metal in creating a Schottky barrier with the conduction band of the $SrTiO_3$ photocatalyst to reduce the band gap energy [42, 43], resulting in enhancing the visible light harvesting ability, facilitating the interfacial electron transfer, accelerating the charge separation, and therefore acting as the photocatalytic active site [46, 47]. The hydrogen production rate increased markedly with increasing Pt loading; but beyond the Pt optimum loading of 0.5 wt.%, it decreased slightly with

increasing Pt loading for both UV and visible light irradiation. These results can be explained in that the Pt has both a positive effect (as aforementioned) and a negative effect on the photocatalytic activity. The negative effect is that at a very high loading of Pt, it can behave as a recombination center between the photo-generated electrons and holes, resulting in the decrease in the photocatalytic activity [28]. From the present results, it can be concluded that an excess amount of Pt (beyond the optimum loading of 0.5 wt.%) increases the probability of a recombination reaction, leading to a decrease in the hydrogen production rate.

5.3.4 Effect of MeOH Volume Fraction and Reaction Temperature

A set of H_2 production experiments under the conditions of a 500 ml of MeOH aqueous solution, 0.5 g of the 0.5 wt.% Pt-loaded $SrTiO_3$ photocatalyst, under UV irradiation, and with various MeOH concentrations (0, 5, 20, 40, 50, 60, 95, and 100 vol.%) and reaction temperatures (15, 30, and 45°C) were performed to observe the effects of MeOH concentration and reaction temperature on the H_2 production behavior of the studied systems to determine the most suitable conditions for hydrogen production from the photocatalytic water splitting using MeOH as the hole scavenger. The dependences of the H_2 production rate and the H_2 production enhancement by MeOH on the MeOH concentration at different reaction temperatures are shown in Figures 5.10(a) and 5.10(b), respectively, while the H_2 production enhancement by MeOH was calculated by the following equation:

The hydrogen production enhancement by MeOH

= (The hydrogen production rate from the aqueous MeOH solution system) – (The hydrogen production rate from pure water system)

The dependence of the initial hydrogen production rate on the reaction temperature are used to calculate the apparent activation energy ($\hat{E}_a$, kJ mol^{-1}) based on two reaction temperature ranges: a low temperature range of 15 to 30°C and a high temperature range of 30 to 45°C. The dependence of the apparent activation energy on the MeOH concentration is shown in Figure 5.10(c). Additionally, in order to elucidate the hydrogen production behavior of the studied systems, the seven main

sets of possible reactions [48-51] for hydrogen production are needed to be considered:

First, photo-generated electrons and holes are produced by the photo-excited reaction:

$$SrTiO_3 + h\upsilon \rightarrow e^- + h^+ \quad (5.1)$$

Second, the H^+ species can be produced by three reactions:

- H_2O is dissociated to produce H^+:

$$H_2O \rightarrow H^+ + OH^- \quad (5.2)$$

and $$H_2O + h^+ \rightarrow H^+ + OH^\bullet \quad (5.3)$$

- MeOH reacts with H_2O and h^+ to produce H^+:

$$CH_3OH + H_2O + 6h^+ \rightarrow CO_2 + 6H^+ \quad (5.4)$$

Third, H_2 is formed by a reduction reaction:

$$2H^+ + 2e^- \rightarrow H_2 \quad (5.5)$$

Fourth, the $OH^\bullet$ species can be produced by the photo-generated holes reacted with the OH^- species:

$$OH^- + h^+ \rightarrow OH^\bullet \quad (5.6)$$

Fifth, O_2 production occurs by the photo-generated holes:

$$2OH^\bullet + 2h^+ \rightarrow O_2 + 2H^+ \quad (5.7)$$

Sixth, H_2O re-production occurs via a backward reaction:

$$O_2 + 4H^+ + 4e^- \rightarrow 2H_2O \quad (5.8)$$

As shown in Figure 5.10(a), an increase in either the MeOH concentration or the reaction temperature results in an increase in the H_2 production rate. For the pure H_2O systems, H_2 is produced from the water decomposition reactions (Equations 5.2 and 5.3) and the subsequent reduction reaction of the H^+ species (Equation 5.5). O_2 is produced from the reaction between the generated $OH^\bullet$ (formed by Equations 5.3 and 5.6) and the photo-generated hole (h^+) (Equation 5.7). For the MeOH aqueous solution systems, the H^+ species is produced from both the H_2O decomposition (Equations 5.2 and 5.3) and MeOH-H_2O-h^+ reaction (Equation 5.4), resulting in the higher amount of H^+ species in the solution, which are possibly

further reduced to H_2, as compared to that of the pure H_2O system. Moreover, the MeOH-H_2O reaction scavenges six photo-generated-holes (h^+) per one mole of MeOH, resulting in the decrease in the O_2 production as well as the backward reaction. Therefore, the MeOH aqueous solution systems show the higher hydrogen production rate than the pure water systems. O_2 and CO_2 are also possibly produced according to Equations 5.7 and 5.4, respectively. However, both O_2 and CO_2 cannot be detected under any given studied conditions. This is possibly because both O_2 and CO_2 are completely dissolved in the solution, due to their much higher water solubility values as compared to that of H_2 (the solubility values of CO_2, O_2, and H_2 in water at 1 atm and 45°C are 800, 38, and 1.35 mg/l, respectively [52]). The effect of the MeOH concentration on H_2 production enhancement by MeOH at both reaction temperatures of 15 and 30°C (Figure 5.10(b)) exhibited the similar trend; H_2 production enhancement increases with increasing MeOH concentration until reaching a plateau after the 20 vol.% MeOH concentration. In contrast, under the reaction temperature of 45°C (Figure 5.10(b)), the H_2 production enhancement continuously increases with increasing MeOH concentration, especially much more significantly at the MeOH concentrations higher than 50 vol.%. When considering the dependence of the H_2 production enhancement by MeOH on the reaction temperature, the H_2 production enhancement by MeOH decreased with increasing reaction temperature from 15 to 45°C, except for the studied conditions of 45°C under high MeOH concentration (of about more than 75 vol.% MeOH fraction).

(a)

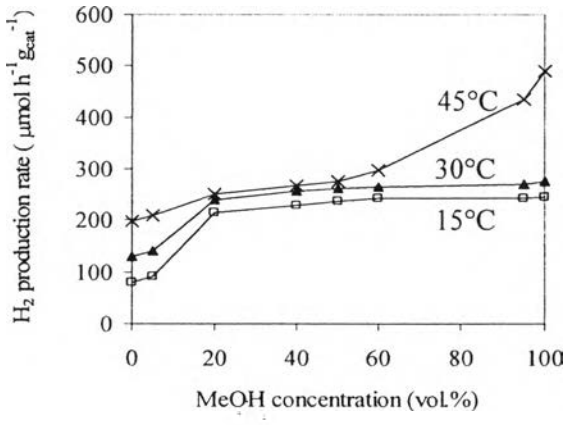

(b)

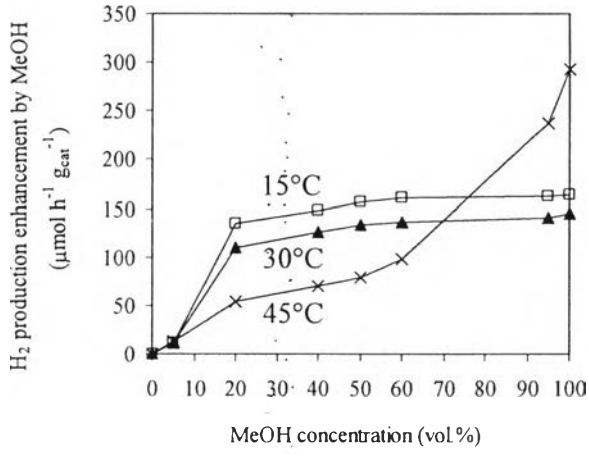

(c)

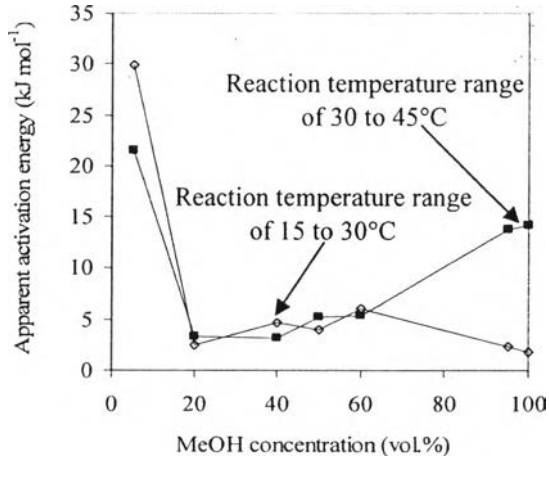

Figure 5.10 Dependences of H_2 production rate (a), H_2 production enhancement by MeOH (b), and apparent activation energy ($\hat{E}_a$) of the photocatalytic water splitting reaction (c) on the MeOH concentration and reaction temperature (studied conditions: 5 h irradiation time, 500 ml of solution, 0.5 g of 0.5 wt.% Pt-loaded $SrTiO_3$ photocatalyst, and UV irradiation).

The dependence of the $\hat{E}_a$ on the MeOH concentration at the two reaction temperature ranges is shown in Figure 5.10(c). For the low reaction temperature range of 15 to 30°C, the $\hat{E}_a$ value significantly decreased with increasing MeOH concentration from 5 to 20 vol.%, and reached a plateau at all MeOH concentrations higher than 20 vol.%. For the high reaction temperature range of 30 to 45°C, the $\hat{E}_a$ value also significantly decreased with increasing MeOH concentration from 5 to 20 vol.%, but reached a plateau only in the MeOH concentration range of 20 to 60 vol.%. At the MeOH concentrations higher than 60 vol.%, the $\hat{E}_a$ value significantly increases with increasing MeOH concentration. The obvious changes in both the H_2 production enhancement by MeOH and the $\hat{E}_a$ value at a high MeOH concentration (greater than 75 vol.%) under a high reaction temperature of 45°C imply that the MeOH-H_2O reaction rate is possibly much improved.

5.3.5 Photocatalyst Durability and Reuse

The time course of H_2 production under the best conditions over the 0.5 wt.% Pt-loaded $SrTiO_3$ photocatalyst under UV irradiation both in terms of the accumulative H_2 production and the instantaneous H_2 production rate is illustrated in Figure 5.11. The H_2 formation was observed after a short irradiation time of about 30 min, proving that the synthesized photocatalysts require a short induction period for hydrogen production, as shown in Figure 5.11(a). The total H_2 production increases with increasing irradiation time, but a decrease in the instantaneous H_2 production rate was simultaneously observed, as shown in Figure 5.11(b). The instantaneous H_2 production rate dropped significantly at initiation, and the decreased trend in the instantaneous H_2 production rate slowed with increasing irradiation time. The big initial drop of the H_2 production rate is possibly due to the adsorption of various intermediate species, which are abruptly produced on the photocatalyst surface, leading to such a rapid decrease in available active sites of the photocatalyst. After 5 h of irradiation, the light was turned off, and the system was left in the dark for a few hours; then the light was turned on to resume the reaction.

(a)

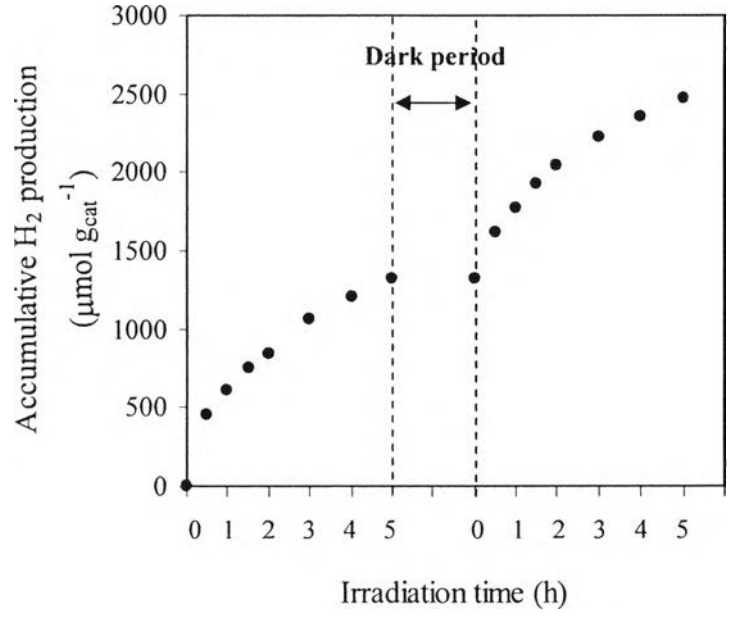

(b)

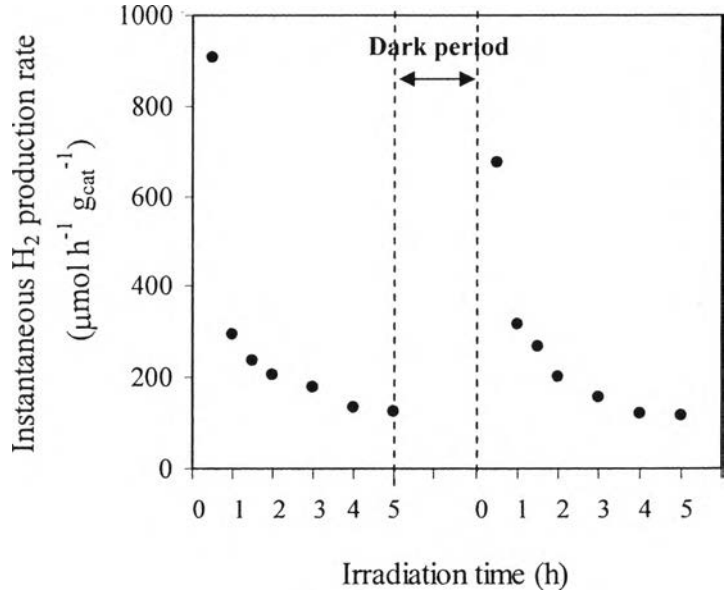

Figure 5.11 Time course of (a) accumulative H_2 production and (b) instantaneous H_2 production rate over the 0.5 wt.% Pt-loaded $SrTiO_3$ photocatalyst under UV irradiation (studied conditions: 500 ml of 50 vol.% MeOH aqueous solution, 0.5 g of photocatalyst, and a reaction temperature of 45°C).

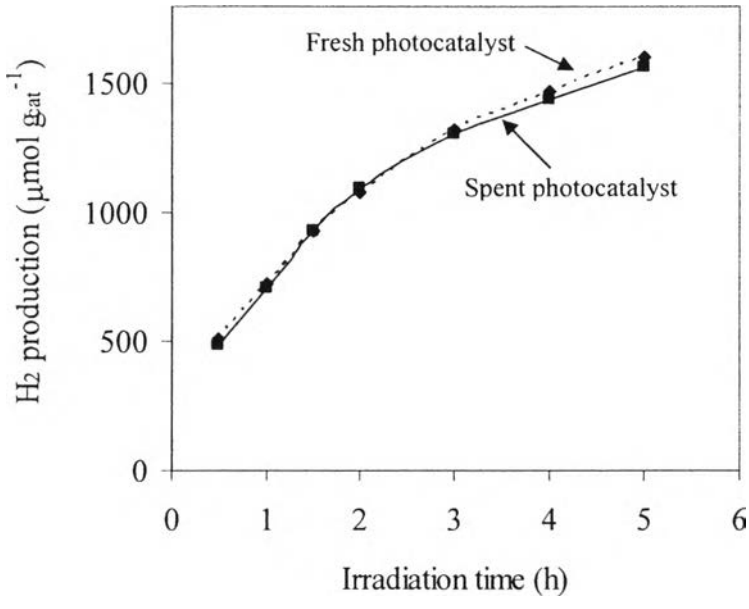

Figure 5.12 Time course of H_2 production over the fresh and spent 0.5 wt.% Pt-loaded $SrTiO_3$ photocatalyst under UV irradiation (studied conditions: 500 ml of 50 vol.% MeOH aqueous solution, 0.5 g of photocatalyst, and a reaction temperature of 45°C).

Figure 5.11 shows that both the accumulative H_2 production and the initial instantaneous H_2 production rate of the second irradiation period were as high as those of the first irradiation period, and their profiles looked similar to those of the first irradiation period (Figure 5.11). These results indicate that the photocatalyst loses some active sites during the reaction by the adsorption of intermediate species. However, when the irradiation is halted and the system is kept in the dark for a few hours, the active sites are possibly recovered by desorption and/or a further reaction of the intermediate species. In addition, the spent photocatalyst was re-tested for its photocatalytic activity performance (Figure 5.12). The spent photocatalyst showed the same photocatalytic H_2 production ability as the fresh photocatalyst. The XRD results of the fresh and the spent photocatalysts indicate that there is no phase change of the spent photocatalyst during the reaction. Therefore, the durability of the photocatalyst is highly acceptable, potentially providing the benefit of the photocatalyst reuse.

5.4 Conclusions

Pristine and Pt-loaded mesoporous-assembled $SrTiO_3$ nanocrystal photocatalysts were successfully synthesized via the sol-gel method with the aid of a structure-directing surfactant under mild conditions. According to the photocatalytic H_2 production results, the photocatalyst structure, in the form of a mesoporous assembly of $SrTiO_3$ nanocrystals, was found to be responsible for the enhancement of the photocatalytic hydrogen production activity. The mesoporous-assembled $SrTiO_3$ nanocrystal photocatalysts exhibited much higher photocatalytic activity than two non-mesoporous-assembled commercial photocatalysts: commercial $SrTiO_3$ and commercial TiO_2 (Degussa P-25). Pt co-catalyst loading was found to enhance the photocatalytic hydrogen production activity of the pristine mesoporous-assembled $SrTiO_3$ nanocrystal photocatalysts. Pt co-catalyst loading decreases the band gap energy of the $SrTiO_3$ photocatalysts, resulting in an increase in the visible light harvesting ability and leading to photocatalytic activity enhancement. However, excessive Pt co-catalyst loading was found to have a negative effect on the photocatalytic activity, and an optimum Pt loading of 0.5 wt.% was required to attain the highest photocatalytic enhancement ability. MeOH exhibited the highest photocatalytic hydrogen production enhancement ability, as compared to the other studied hole scavengers. MeOH behaves as both a hole scavenger to enhance H_2 production and a reactant for providing the H^+ species to form H_2, depending upon the system conditions. The most suitable system conditions for H_2 production from water splitting in this work were a 0.5 wt.% Pt-loaded mesoporous-assembled $SrTiO_3$ nanocrystal photocatalyst, a 50 vol.% MeOH aqueous solution, and a 45°C reaction temperature. This system provided the average hydrogen production rates of 276 and 188 μmol h^{-1} g_{cat}^{-1}, with the quantum efficiencies of 1.9 and 0.9 %, under UV and visible light irradiation, respectively.

5.5 Acknowledgments

This work was supported by a Project on Faculty Development in Shortage Area Scholarship (Thailand); Thailand Research Fund (TRF) and the Commission on Higher Education (Thailand); the Research Unit of Petrochemical and Environmental Catalysis, Chulalongkorn University (Thailand); and the Sustainable Petroleum and Petrochemicals Research Unit, Center for Petroleum, Petrochemicals, and Advanced Materials, Chulalongkorn University (Thailand).

5.6 References

[1] A. L. Linsebigler, G. Lu, J. T. Yates, Chem. Rev. 95 (1995) 735.

[2] H. Gerischer, J. Electroanal. Chem. 82 (1977) 133.

[3] S. Ikeda, T.K. Itani, K. Nango, M. Matsumura, Catal. Lett. 98 (2004) 229.

[4] J. R. Bolton, Sol. Energ. 57 (1996) 37.

[5] M. Ashokkumar, Int. J. Hydrogen Energ. 23 (1998) 427.

[6] Z. Zou, J. Ye, K. Sayama, H. Arakawa, Nature 414 (2001) 625.

[7] Z. Zou, J. Ye, K. Sayama, H. Arakawa, Int. J. Hydrogen Energ. 28 (2003) 663.

[8] S. Licht, B. Wang, S. Mukerji, I. T. Soga, M. Umeno, H. Tributsch, J. Phys. Chem. B 104 (2000) 8920.

[9] K. Sayama, H. Arakawa, Chem. Commun. 2 (1992) 150.

[10] K. Sayama, H. Arakawa, J. Photochem. Photobiol. A: Chem. 77 (1994) 243.

[11] K. Sayama, H. Arakawa, J. Photochem. Photobiol. A: Chem. 94 (1996) 67.

[12] K. Sayama, H. Arakawa, Catal. Surv. Jpn. 4 (2000) 75.

[13] T. Takata, A. Tanaka, M. Hara, J. N. Kondo, K. Domen, Catal. Today 44 (1998) 17.

[14] R. Abe, K. Sayama, H. Arakawa, Chem. Phys. Lett. 371 (2003) 360.

[15] Y. X. Li, G. X. Lu, S. B. Li, Chemosphere 52 (2003) 843.

[16] T. R. N. Kutty, M. Avudaithai, Mater. Res. Bull. 23 (1988) 725.

[17] K. Sayama, K. Mukasa, R. Abe, Y. Abe, H. Arakawa, J. Photochem. Photobiol. A: Chem. 148 (2002) 71.

[18] J. W. Liu, G. Chen, Z. H. Li, Z. G. Zhang, J. Solid State Chem. 179 (2006) 3704.

[19] J. Wang, S. Yin, M. Komatus, T. Sato, J. Eur. Ceram. Soc. 25 (2005) 3207.

[20] V. Subramanian, R. K. Roeder, E. E. Wolf, Ind. Eng. Chem. Res. 45 (2006) 2187.

[21] T. Ohno, M. Akiyoshi, T. Umebayashi, K. Asai, T. Mitsui, M. Matsumura, Appl. Catal. A: Gen. 265 (2004) 115.

[22] T. Ohno, T. Tsubota, Y. Nakamura, K. Sayama, Appl. Catal. A: Gen. 288 (2005) 74.

[23] T. Puangpetch, T. Sreethawong, S. Yoshikawa, S. Chavadej. J. Mol. Catal. A: Chem. 287 (2008) 70.

[24] Y. Zhang, A. Weidenkaff, A. Reller, Mater. Lett. 54 (2002) 375.

[25] T. Sreethawong, Y. Suzuki, S. Yoshikawa, Int. J. Hydrogen Energ. 30 (2005) 1053.

[26] T. Sreethawong, S. Ngamsinlapasathian, Y. Suzuki, S. Yoshikawa, J. Mol. Catal. A: Chem. 235 (2005) 1.

[27] T. Sreethawong, Y. Yamada, T. Kobayashi, S. Yoshikawa, J. Mol. Catal. A: Chem. 241 (2005) 23.

[28] T. Sreethawong, S. Yoshikawa, Int. J. Hydrogen Energ. 31 (2006) 786.

[29] T. Ishii, H. Kato, A. Kudo, J. Photochem. Photobiol. A: Chem. 163 (2004) 181.

[30] R. Konta, T. Ishii, H. Kato, A. Kudo, J. Phys. Chem. B 108 (2004) 8992.

[31] A. Kudo, Int. J. Hydrogen Energ. 31 (2006) 197.

[32] Z. Ahmad, Principles of Corrosion Engineering and Corrosion Control, Butterworth Heinemann, Saudi Arabia, 2006.

[33] T. Kida, G. Guan, N. Yamada, T. Ma, K. Kimura, A. Yoshida, Int. J. Hydrogen Energ. 29 (2004) 269.

[34] H. Yang, L. Guo, W. Yan , H. Liu, J. Power Sources 159 (2006) 1305.

[35] B. D. Cullity, Elements of X-ray Diffraction, Addison-Wesley Pub. Co., Reading, MA, 1978.

[36] P. V. Kamat, Handbook of Nanostructured Materials and Nanotechnology: Semiconductor Nanoparticles, Academic Press, New York, 1999.

[37] J. V. Smith (Ed.), X-Ray Powder Data File, American Society for Testing Materials, Philadelphia, PA, 1960.

[38] F. Rouquerol, J. Rouquerol, K. Sing, Adsorption by Powders and Porous Solids: Principles, Methodology and Applications, Academic Press, San Diego, 1999.

[39] X. Fu, Y. Wang, N. Wu, L. Gui, Y. Tang, J. Mater. Chem. 13 (2003) 1192.

[40] M. Karger, M. Schilling, Phys. Rev. B. 71 (2005) 174.

[41] S. Hagashimoto, Y. Ushiroda, M. Azuma, H. Ohue, Catal. Today 132 (2008) 165.

[42] N. Serpone, E. Pelizzetti, Photocatalysis-Fumdamentals and applications, Eds, Wiley-Interscience, New York, 1989.

[43] D. Hufschmidt, D. Bahnemann, J.J. Testa, C.A. Emilio, M.I. Litter, J. Photochem. Photobiol. A: Chem. 148 (2002) 223.

[44] T. Sreethawong, T. Puangpetch, S. Chavadej, S. Yoshikawa, J. Power Sources 165 (2007) 861.

[45] A. Hameed, M. A. Gondal, J. Mol. Catal. A: Chem. 233 (2005) 35.

[46] T. Kawai, T. Sakata, J. Chem. Soc. Chem. Commun. 15 (1980) 694.

[47] T. Sakata, T. Kawai, Chem. Phys. Lett. 80 (1981) 341.

[48] J. C. Brown, E. Gulari, Catal. Commun. 5 (2004) 431.

[49] J. Chen, D. F. Ollis, W. H. Rulkens, H. Bruning, Water Res. 33 (1999) 669.

[50] J. W. Park, M. Kang, Int. J. Hydrogen Energ. 32 (2007) 4840.

[51] T. A. Niyazi, P. Jai, J. Eng. Env. Sci. 29 (2005) 95

[52] http://www.engineeringtoolbox.com/gases-solubility-water-d